

Analysis and Control of the Near-Wake Flow over a Square-Back Geometry

Mathieu Rouméas⁺, Patrick Gilliéron⁺ & Azeddine Kourta^{*}

⁺*Renault, Direction de la Recherche, Groupe "Mécanique des Fluides & Aérodynamique"*
1, Avenue du Golf 78288 Guyancourt cedex, France

^{*}*Institut de Mécanique des Fluides de Toulouse, Groupe EMT2*
Allée du Professeur Camille Soula 31400 Toulouse, France

Abstract

A 3D numerical simulation, based on the Lattice Boltzmann Method is carried out on the near-wake flow behind a generic square-back blunt body to analyze and establish a method to control the near-wake flow. The flow topology is described by the velocity and the pressure fields. The influence of the wake vortices on the aerodynamic drag is clarified and quantified. In order to reduce this drag, an active open-loop flow control is applied by continuous blowing devices distributed around the base periphery. The blowing effect on the behind body flow is a reduction of the wake section and of the total pressure loss in the wake and an increase of the static pressure on the base of the square body. This control leads to a significant drag reduction of $\Delta C_x = -29\%$ with a blowing velocity of $1.5V_0$. The efficiency is then studied, and we found that the most efficient control is obtained for a blowing velocity of $0.5V_0$ and a jet angle of 45° . In this case, a 20% drag reduction is obtained, and the energy needed to control the system is 7 times lower than the energy saved by the control.

Keywords: Lattice Boltzmann Method / 3D Square-Back / Drag reduction / Active control / Blowing

Nomenclature

A	=	Wake section
C_p	=	Static pressure loss coefficient
C_{pi}	=	Total pressure loss coefficient
C_x	=	Drag coefficient
e	=	Width of the slot
F_x	=	Aerodynamic drag
f_i	=	Lattice Boltzmann distribution function

H	=	Height of the simplified car geometry
h	=	Height of the underbody flow
k	=	Turbulent kinetic energy
L	=	Length of the simplified car geometry
L_0	=	Reference length
P	=	Static pressure
P_i	=	Total pressure
P_{i_0}	=	Reference total pressure
Re	=	Reynolds number
u^+	=	Friction velocity
V_0	=	Reference velocity
V_b	=	Blowing velocity
(V_x, V_y, V_z)	=	X, Y, Z components of the local velocity
V_i	=	Lattice Boltzmann distribution velocity
w	=	Width of the simplified car geometry
$(\omega_x, \omega_y, \omega_z)$	=	X, Y, Z components of the local vorticity
(x, y, z)	=	Coordinate system related to the simplified car geometry
y^+	=	Wall coordinate
ρ	=	Density
ρ_0	=	Reference density
ν	=	Kinematic viscosity
ν_t	=	Turbulent eddy viscosity
θ	=	Inclination of the blowing velocity
ε	=	Turbulent dissipation
τ_p	=	Wall shear stress
ζ	=	Deformation rate
η	=	Efficient coefficient
S	=	Deformation tensor
S_c	=	Surface of the vehicle

I. Introduction

New constraints in terms of pollutant emissions and fuel consumption are warranting the development of new flow control devices capable of reducing the aerodynamic drag of motorized vehicles. In this context, the objective is to modify the near wall flow and thereby to limit the development and dissipation of the separated vortices that contribute to the aerodynamic drag.

Active solutions need an external energy source in order to control the flow around the vehicle without necessarily interfering with its shape. Many flow control techniques [1] have been developed both in research and industrial laboratories, and significant results have been found on simplified geometries [2]. For instance, blowing devices installed on an ONERA D profile are capable of displacing or even eliminating flow separations [3]. Similar results have been obtained by Tensi *et al.* [4] on a cylindrical body. Many studies demonstrate the promising results of suction and/or blowing techniques in the reduction of the aerodynamic drag of an automotive vehicle [5].

The implementation of such solutions on an automotive vehicle, however, requires a better understanding of the physical phenomena encountered in the near-wake flow, and an identification of the parameters that contribute to the aerodynamic drag.

The flow around a bluff body is, in general, associated with flow separation, reattachment, and unsteady vortex formation in the wake region. Such complex flow phenomena become more complicated as the body is located close to the ground. The gap between the body and the wall changes the flow characteristics such as, vortex periodicity and the mass flux through the gap, etc. For a ground vehicle with smooth underbody, the mean drag coefficient decreases as the ground clearance is increased. Thus the flow around a bluff body close to the ground has practical importance to automobiles since they are supported close to the ground by wheels. Therefore, it is important to carry out fundamental research into the flow around simple shaped bodies close to the ground. Flow around vehicles has been principally studied experimentally [6-12]. Actually, few numerical studies have been done in the configuration because of the poor prediction of this flow using Reynolds Averaged Navier Stokes (RANS) modelling. Large Eddy Simulation (LES) has been also used [13,14] and with fine resolution by approaching Direct Numerical Simulation (DNS) near the wall, results are better and in agreement with experimental data. The purpose of this paper is to present Lattice Boltzmann computations to characterise this flow and also to apply drag reduction control.

To reduce the aerodynamic drag of automotive vehicles, by local modification of the flow in a given design, and to have a negligible impact on the vehicle geometry, the key issue consists in reducing the transversal wake section, increasing the static pressure distribution on the rear part of the vehicle and reducing the total pressure losses in the near wake flow [15]. One solution consists in reproducing the impact of separated elements [16] on the near-wake flow, by using continuous blowing devices located on the rear part of the geometry.

In the present study, according to bibliographic results [4, 17], an open loop active flow control by continuous blowing slots is thus tested on a simplified square-back geometry. In this paper, a 3D numerical method is presented in the section II. The results obtained with and without control are then successively analyzed in the remaining parts of this paper (section III).

II. Numerical simulation

II.1 Computation code

The numerical method used in a previous paper [18], to compute successfully the flow around the rear part of an Ahmed body, is applied here. It consists of a 3D numerical simulation based on the Powerflow code with a Lattice Boltzmann Method (LBM) [19, 20]. This method is based on microscopic models and mesoscopic kinetic equations. The fundamental principle of the LBM is to construct simplified kinetic models that incorporate the essential physics of microscopic or mesoscopic processes such that the macroscopic-averaged properties conform to the desired macroscopic equations. The basic premise for using these simplified kinetic-type methods for macroscopic fluid flows is that the macroscopic fluid dynamics are the result of the collective behavior of many microscopic particles in the system and that the macroscopic dynamics are not sensitive to the underlying details [18,21].

The fluid particles are distributed on a Cartesian lattice of computation nodes, described on Fig. 1. For each lattice node, a distribution function $[f_i]_{i=1\dots N}$ is associated with a discrete velocity distribution $[\vec{V}_i]_{i=1\dots N}$ representing N possible velocities of motion (Fig. 1). One particle placed on one node may stay at this node (energy level 0: $\bar{e} = 0$, represented by a triangle (figure 1)), move toward an adjacent node in horizontal or vertical plane (energy level 1: $\bar{e} = 1$, circle) or move to a farthest node (energy level 2: $\bar{e} = 2$, black dot). The model gives 34 possible combinations and is called 34 velocities model (2 possibilities for level 0, 18 for level 1 and 14 for level 2). More details concerning the algorithm can be found in [18-23]. The kinetic energy is then given by $\bar{e} = \frac{1}{2} \sum_{i=1}^N V_i^2$.

The general algorithm for the LBM is thus defined in 4 stages. The first consists in propagating the distribution function in time t+1 [25, 26]. In the second stage, the collisions between the particles are modelled. The collision operator is then applied to time t-1. The third stage consists in determining the associated values of density and density momentum. Finally, the fourth stage consists in initiating iteration on the basis of the macroscopic values determined in the third stage.

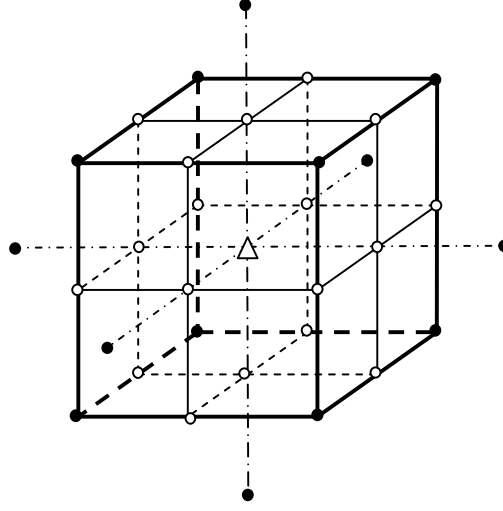


Fig. 1: Definition of a velocity lattice with 34 velocities on 3 energy levels
 (\triangle level 0, \circ level 1, \bullet level 2), Chen et al. [24]

Similarly to all numerical space-time discretization methods, the LBM is not capable of resolving all turbulence scales. The computation code therefore uses a turbulence model which introduces a turbulent viscosity into the initial set of equations.

This model is an extension of the k- ϵ RNG [27] model applied to the same lattice as that used for the Boltzmann equation and based on the use of finite second-order differences (Lax-Wendroff) and a time-explicit scheme [28]. In this model, the Reynolds tensor is modelled by means of a Boussinesq approximation:

$$\tau_{ij} = 2\mu_t S_{ij} - \frac{2}{3}\rho k \delta_{ij} \quad (1)$$

in which the turbulent viscosity is defined by $\nu_t = \frac{\mu_t}{\rho} = C_\mu \frac{k^2}{\epsilon}$. The equations for k and ϵ are defined by:

$$\frac{Dk}{Dt} = \frac{\partial}{\partial x_j} \left[\left(\frac{v}{\sigma_{k0}} + \frac{\nu_t}{\sigma_{kt}} \right) \frac{\partial k}{\partial x_j} \right] + \nu_t |S|^2 - \epsilon \quad (2)$$

$$\frac{D\epsilon}{Dt} = \frac{\partial}{\partial x_j} \left[\left(\frac{v}{\sigma_{\epsilon0}} + \frac{\nu_t}{\sigma_{\epsilon t}} \right) \frac{\partial \epsilon}{\partial x_j} \right] + C_{\epsilon 1} \nu_t \frac{\epsilon}{k} |S|^2 - \left[C_{\epsilon 2} + f_{\text{RNG}} C_\mu \frac{\eta^3 (1 - \eta/\eta_0)}{1 + \beta \eta^3} \right] \frac{\epsilon^2}{k} \quad (3)$$

where η denotes the non dimensional deformation rate such that $\eta = \frac{|S|k}{\epsilon}$ and $|S|$ is the deformation rate directly

calculated according to the LBM. The closing values of the model constants are indicated by Yakhot and Orszag [27]:

$C_\mu = 0.085$	$C_{\varepsilon 1} = 1.42$	$C_{\varepsilon 2} = 1.92$	$\sigma_{k0} = 1$	$\sigma_{\varepsilon 0} = 1$
$\sigma_{kt} = 1$	$\sigma_{\varepsilon t} = 0,719$	$\eta_0 = 4.38$	$\beta = 0.012$	$f_{RNG} = 1$

Close to the wall, a specific velocity law is applied to limit the computational workload [29]. Then the velocity follows the logarithmic law described in Eq. (4):

$\frac{u_y}{u^+} = \frac{1}{\kappa} \log\left(\frac{y^+}{\zeta}\right) + C$	(4)
---	-----

with:
$$\begin{cases} u^+ = \sqrt{\frac{\tau_p}{\rho}} \\ y^+ = y \frac{u^+}{\nu} \end{cases} \quad \zeta = 1 + a \left(h \frac{\partial P}{\partial x} \right)^b \quad \text{and} \quad h = \frac{L_0}{\rho_0 V_0^2}$$

in which u_y represents the tangential velocity, κ the Karman constant ($\kappa=0.41$), C a constant applied by the model ($C=5$), τ_p the wall shear stress, y and u^+ the distance and friction velocity on the wall respectively, ν the kinematic viscosity and ζ a correction term to make allowance for the adverse pressure gradient. This equation is applicable for values of y^+ between 30 and 300. a and b are two empirical constants.

A validation of this numerical method can be found in the literature on numerous applications (Pipe flow [28] flow past a cylinder [29], NACA 12 profile [30]). It can be also found in our previous paper related to the Ahmed Body [18]. The difference between, our previous study and this one is that instead of an Ahmed body we use a square-back geometry here. The goal is to focus on the different mechanisms occurring in each case and to evaluate and improve the drag contribution of the rear part of the car bodies.

II.2 Numerical simulation protocol

In order to limit the computation time, the front part is not represented. The flow separations developing on the front (rounded or sharp) surface are not represented; the simulation exclusively focuses on the back of the bluff body as it was done before for the Ahmed body [21]. The consequence of this limitation is that the boundary layer thicknesses on roof and sides may be not exactly reproduced. Hence, to obtain the main important characteristics at

the rear body (the separation and vortices), the length of the computed body is fixed in such way that the boundary layer thickness at the end of the roof is equivalent to the one of the complete body.

The geometry is defined by its length ($L=1.044$ m), its width ($w=0.389$ m) and its height ($H=0.288$ m) (Fig. 2). This bluff body is located at $h=5.10^{-2}$ m from the ground (Fig. 2) to model the flow field under the body and the lateral secondary flow. The geometry is located in a rectangular numerical section of length, width and height equal to $30L$, $40w$ and $30H$ respectively (Fig. 2). These dimensions ensure that there is no interaction between the development of the near-wake and the boundary conditions imposed at the limit of the computational domain. The outlet condition, downstream from the geometry and on the upper part, is a free flow condition on pressure and velocity [31]. The flow is advected from left to right and a uniform velocity $V_0=40\text{m}\cdot\text{s}^{-1}$ is applied to the left-hand surface of the simulation domain (Dirichlet velocity condition at the inlet). The Reynolds number associated with length L of the geometry is $Re=2.8\cdot 10^6$. Finally, symmetry conditions are applied on the side surfaces of the simulation domain [31-33].

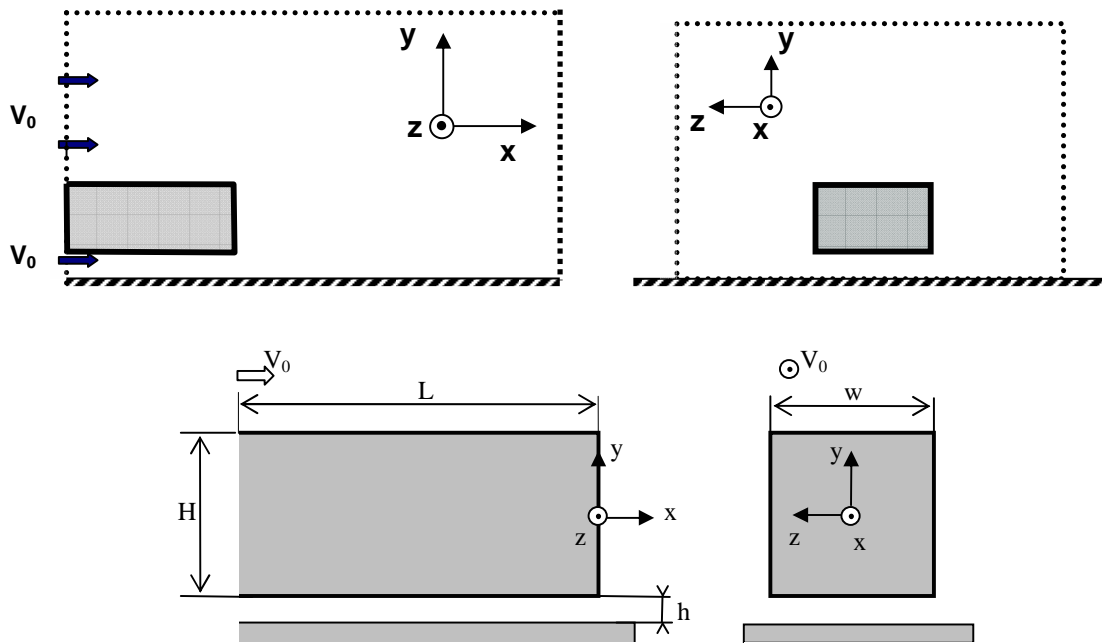


Fig. 2: Computational domain (top) and the square-back geometry(bottom)

The square-back geometry surface is meshed by using approximately $1.2\cdot 10^6$ cells. At the end of the roof, the first computational node is located at $y^+ \sim 30$ from the wall. The most refined domains are thus located in areas generating flow separations, close to the periphery of the body (Fig. 3). The number of volume cells in the computational domain is $16.7\cdot 10^6$ of which $15\cdot 10^6$ are distributed near the body.

The simulation volume is subdivided into parallelepiped domains. Inside each domain, the volume mesh is cartesian, uniform and the resolution is halved as it moves away from the surface. Each block B_k is associated with a resolution level δx_k , defined by $\delta x_k = 2^k \cdot \delta x_0$, δx_0 represents the most refined resolution, i.e. the size of an elementary computation cube in the block having the highest resolution. The finest domain contains $0.25 \cdot 10^{-3} \times 0.25 \cdot 10^{-3} \text{ m}^2$ grids.

In the present case, 12 levels (0 to 11) of blocks have been created: the fourth most refined levels are located in areas generating high gradient and flow separations, close to the body (B_0 , B_1 , B_2 and B_3) (Fig. 3). The square body is hence completely contained in block B_3 , with resolution $\delta x_3 = 2 \cdot 10^{-3} \text{ m}$.

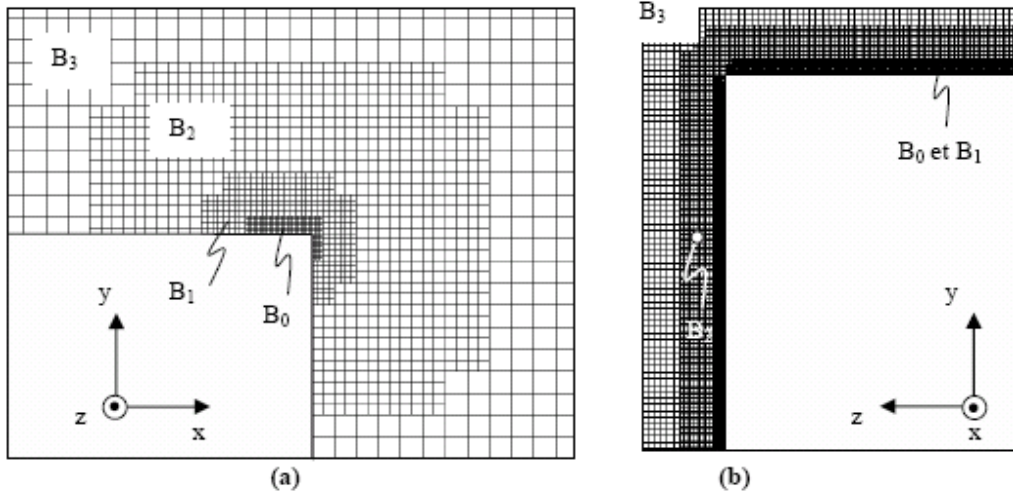


Fig. 3: Mesh close to the separation: (a) longitudinal median plane, (b) transverse plane

According to the CFL criterion, the global computation time step is equal to $1.354 \cdot 10^{-6} \text{ s}$ and the simulation is conducted over 500,000 iterations, corresponding to 0.7 s of real time. Convergence is reached after 50,000 time steps and the numerical results are averaged on 0.61 s (50,000 to 500,000 iterations).

From one block to the next one (B_i to B_{i+1}), the mesh density is divided by 2. The time step is defined by

$$\Delta t = \text{CFL} \cdot c_s \left| \frac{\vec{\Delta x}}{\Delta t} \right|, \text{ where } c_s \text{ is the sound celerity, in this case given by } c_s = \sqrt{\frac{D+2}{D}} T \left| \frac{\vec{\Delta x}}{\Delta t} \right|, \text{ D the degree of}$$

freedom equal to 4 and $|\overline{\Delta x}|$ is the cell size. From this expression it can be easily obtained that the CFL number is

$$\text{thus equal to } 0.794 \left(CFL = c_s \frac{\Delta t}{\Delta x} = \sqrt{\frac{D+2}{D}} T \approx 0.794 \right).$$

The CFL number is kept constant all over the computational domain which means that the local time step is proportional to the cell size. So the time step is doubled from one block to the next one. This means that the local time step is different at each bloc. For each global time step, the number of internal iteration is different from one bloc to another. This Dual Time Stepping procedure increases the convergence and for the present computation only 50.000 iterations are needed. The convergence is based on the drag coefficient error. The convergence is reached when the relative error is smaller than 1%.

In the following sections, the analysis is first conducted without control and the observed flow topology is compared to experimental and numerical results found in the literature, in order to validate the numerical simulation. The blowing jets, whose distribution is given, are then applied and the results obtained with and without control are analyzed to define the influence of the blowing devices.

III. Numerical Results

III.1 Topology of the flow without control

For this kind of geometry, drag reduction depends on the wake surface and pressure loss distribution. For this reason, the flow topology analysis is conducted on total and static pressure loss fields completed by velocity and vorticity profiles measured in the near-wake flow, in the longitudinal median plane ($z=0$).

The streamlines emanating from the roof, the underbody, and the side walls of the body separate on the rear edges of the base of the square and form together a circular vortex ring (W in Fig. 4), which is typical for the wake of a square-back body. This circular vortex ring, already observed experimentally [34, 35] and numerically [36], is the location of significant total pressure losses, highlighted in Fig. 4 by a total pressure loss iso-surface of coefficient C_{pi} equal to 1.17, where:

$$C_{pi} = \frac{P_{i0} - P_i}{\frac{1}{2} \rho V_0^2} \quad (5)$$

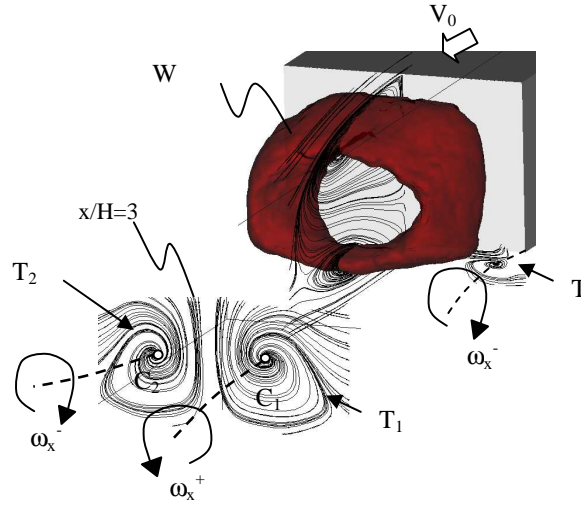


Fig. 4: Near-wake flow topology over a simplified blunt body (iso-surface $C_{pi}=1.17$).

Due to the interaction between the transversal vortex W and the main flow in the longitudinal direction, after the closure of the separation bubble, a pair of counter-rotating longitudinal vortices is formed [33-35] (T_1 and T_2 on fig. 4). These vortices appear at $x/H=1.4$ and were detected all along the measurement domain ($x/H=7$). Similar results have been obtained on a square-back vehicle [36], but with however two pairs of counter-rotating horse-shoe shaped longitudinal vortices. We could also distinguish in figure (4), another pair of counter-rotating longitudinal vortices supplied by the underbody flow and detected near the bottom body corners. Only one of them is visible in figure 4 (T). These vortices dissipate very quickly and are no longer apparent at $x/H=1.4$.

In the plane (x, y) , at $z=0$, the vortex ring W corresponds to a pair of counter-rotating vortices (centred in F_1 and F_2 , Fig. 5). The upper structure is much larger than the lower one. The attachment point N thus appears at the bottom of the base ($y/H=-0.2$ in Fig. 5). This asymmetry has also been observed experimentally [34] and numerically [35], on a similar geometry. The small ground clearance and the lateral secondary flow [37] actually suppress the flow entering the wake from under the body (Fig. 5). This asymmetry can explain the differences already noted by Hucho [36]. Indeed, the lower vortex (centred in F_2) appears to be less energetic. Further downstream, the streamlines also reveal a singular saddle point S at $x/H=1.35$ (Fig. 5).

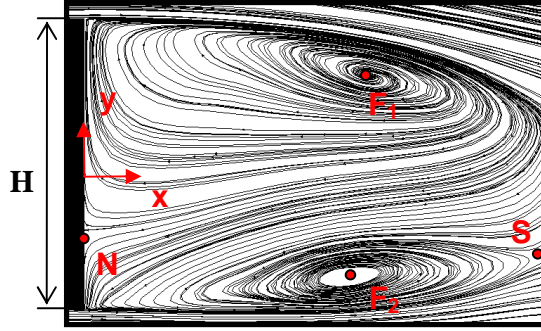


Fig. 5: Time-averaged streamlines field in the wake, on the symmetry plane.

The vorticity profiles (ω_z defined by equation (6)), in the plane $z=0$, at different x/H , are plotted on Fig. 6. Notice that the vorticity peaks correspond to the position of the shear layer issuing from the sharp rear edges. Moving downstream, the peak position moves towards the median plane ($y=0$) and its intensity decreases. These behaviours correspond to the expansion of shear layers separating from the top and bottom surface of the vehicle and there interaction.

$$\omega_z = \frac{1}{2} \left(\frac{\partial V_y}{\partial x} - \frac{\partial V_x}{\partial y} \right) \quad (6)$$

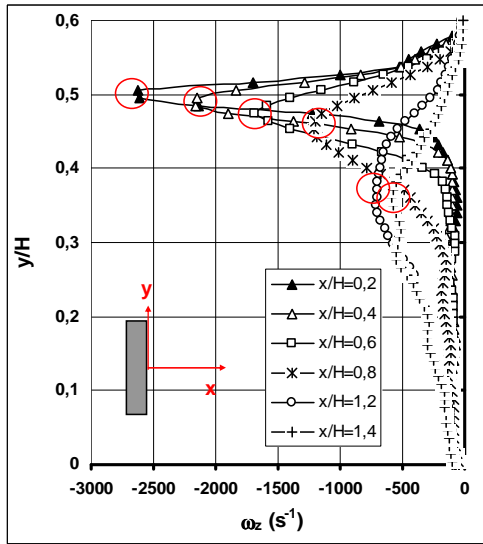


Fig. 6: Vertical vorticity (ω) profiles, measured along the longitudinal median plane at different x/H

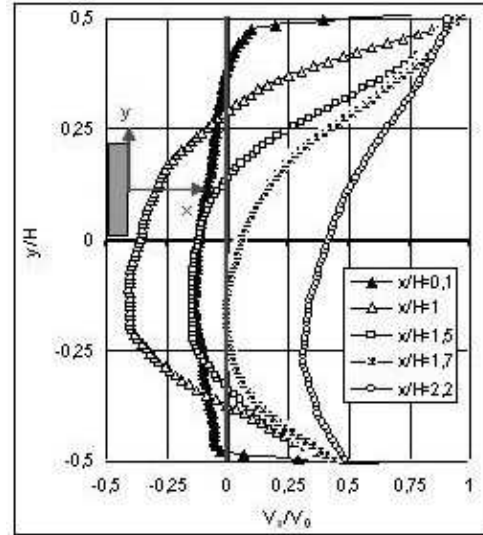


Fig. 7: Vertical longitudinal velocity profiles, measured along the longitudinal median plane at different x/H

The longitudinal velocity profiles at the same positions are plotted on fig. 7. The backward flow, already observed in Fig. 4 and Fig. 5, is quantified. The longitudinal velocity is negative close to the median plane ($y=0$) and its minimum value, approximately equal to $V_{x\min}=-0.4$, appears at $x/H=1$ and for $y/H=-0.1$. Moving towards the base of

the body ($x/H=0.1$), the backward velocity decreases due to the wall effect, and $V_{x_{\min}}$ is close to $-0.06 V_0$ over the whole height of the base ($-0.5 < y/H < 0.5$). Moving downstream, the backward flow decreases ($V_{x_{\min}} \sim -0.15 V_0$ at $y/H=-0.1$, for $x/H=1.5$) and goes to zero ($V_{x_{\min}}=0$ at $y/H=-0.2$, for $x/H=1.7$).

The results presented in Fig. 6 and Fig. 7 are characteristic of the development and dissipation of a recirculation zone in the square-back vehicle wake.

Using the λ_2 criterion, we could visualize the time evolution of vortices of the shear layers developing over and under the recirculation zone [21]. This behaviour is the same as in the shear layer developed in the near wake of a circular cylinder [38] or behind an obstacle [39]. The Strouhal number defined by $S_{\omega} = \frac{f * \delta_{\omega}}{U_c}$ is computed, where

δ_w is the shear layer thickness, U_c is the vortices' convective velocity and f is the estimated Kelvin-Helmholtz frequency obtained by spectral analysis. The estimated convective velocity is 20 m/s and the shear layer thickness is 0.03 m at $x/H=0.035$. With these values the obtained Strouhal number is equal to 0.27. It corresponds to a typical Strouhal number associated to Kelvin-Helmholtz instability. Regarding previous works this value is in the range of 0.25 to 0.33.

III.2 Topology of the flow with control

The control setup consists of 4 slots of width $e=10^{-3}$ m located at the base periphery, and respectively tangential to the roof plane, the underbody and the side walls (Fig. 8.a). Lengths l_1 and l_2 of the vertical and horizontal slots are equal to $l_1/H=0.93$ and $l_2/H=1.32$, respectively. A uniform velocity condition is applied at the slot exit: the blowing velocity V_b is set to $1.5V_0$ and its direction forms an angle θ with respect to the base plane (Fig. 8.b). The blowing devices effects on the time-averaged aerodynamic drag coefficients are first analysed. The static and total pressure coefficient fields, obtained with and without control, are then used to clarify the mechanism of the blowing control.

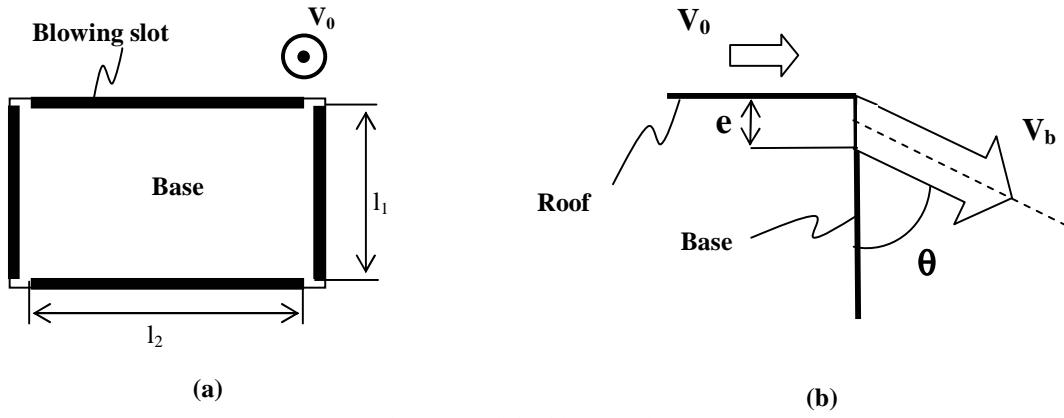


Fig. 8: Schematic of the blowing devices set up

The aerodynamic drag force F_x is computed during the simulation. It is obtained by adding the viscous and pressure forces around the full three-dimensional geometry at each iteration. Then, it is time averaged to obtain the drag. The time-averaged drag coefficient evolution, as function of inclination θ is presented in Fig. 9, with:

$$C_x = \frac{F_x}{\frac{1}{2} \rho V_0^2 H w} \quad (7)$$

The results reveal a minimum in the drag coefficient at $\theta_0=45^\circ$. At this orientation, the associated drag reduction compared to the reference case without control, corresponds to $\Delta C_x=-28.9\%$. The drag reduction then rapidly decreases as the angle θ decreases (blowing jet tangential to the base plane) or increases (blowing jet tangential to the longitudinal direction). The associated drag reductions still remain significant: $\Delta C_x=-17.9\%$ at $\theta=30^\circ$, $\Delta C_x=-20.8\%$ at $\theta=60^\circ$ and $\Delta C_x=-17.1\%$ at $\theta=75^\circ$. The error-bar line segments in Figs.10 are the standard deviation (rms) of the time averaged drag coefficient.

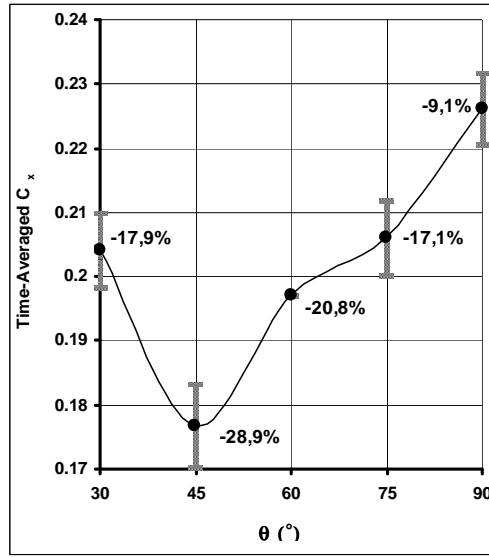


Fig. 9: Time-averaged aerodynamic drag evolution, as a function of blowing velocity orientation θ

The velocity and streamline time-averaged fields are measured at the upper edge of the base in the longitudinal median plane ($z=0$), as shown in Fig. 10. At $\theta=45^\circ$ and $\theta=60^\circ$, the results show that the streamlines are deviated by 45° (respectively 60°) with respect to the base plane, in the vicinity of the separation line (Fig. 10). The momentum introduced into the flow therefore acts as a separated element and inclines the streamlines. Because of the main flow, the streamlines then tend to become realigned with the upstream direction V_0 , although a residual deviation angle remains visible in the wake (β in fig. 10). Further downstream, this residual deviation, close to $\beta=10^\circ$ for $\theta=45^\circ$ and $\theta=60^\circ$, induces a transversal wake section reduction, which will be discussed in the following section. At $\theta=30^\circ$ (Fig. 10), the momentum introduced in the vertical direction induces the formation of a secondary transversal vortex (centred in F_3 in Fig. 10). The anticlockwise rotation of the fluid tends to realign the streamlines with the upstream direction, and the residual deviation β tends to $\beta=5^\circ$. The formation of this structure also induces total pressure losses, which contribute to increase the aerodynamic drag coefficient, as shown in Fig. 9.

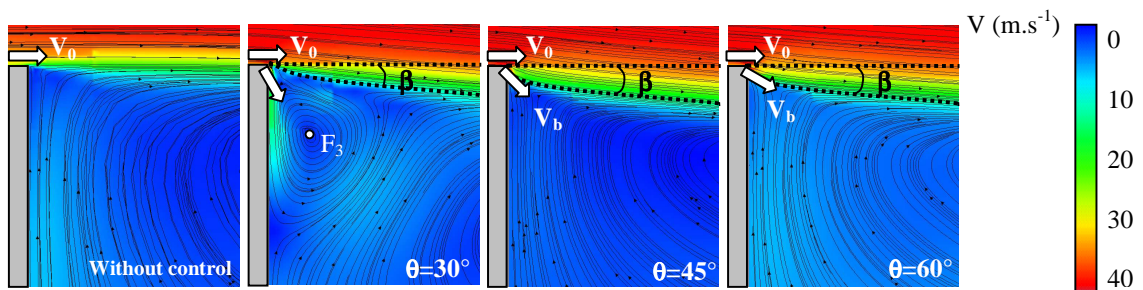


Fig. 10: Velocity and streamline fields measured at the upper edge of the base in the longitudinal median plane

The application of blowing control devices leads to a modification of the near-wake flow topology as shown in Fig. 11, representing the streamline fields in the longitudinal median plane ($z=0$). At $\theta=45^\circ$ or $\theta=60^\circ$, the asymmetry observed in Fig. 5 (without control) disappears (see Fig. 11.b and Fig. 11.c). The momentum introduced into the flow creates an important shear effect on the base periphery, and that tends to induce a displacement of the recirculation. Hence, the shear layers emanating from the top and the bottom of the base seem identical and the counter-rotating vortices which develop on the base become quasi-symmetrical (Fig. 11.b and Fig. 11.c). The attachment point N thus appears close to the base center ($y/h=0$, Fig. 11.b and 11.c) and the vortical centers F_1 and F_2 become quasi-symmetrical with respect to the median plane ($y=0$). On the other hand, when the blowing angle is less than 45° ($\theta=30^\circ$ fig. 11.a), the momentum applied in the longitudinal direction decreases and the induced shear effect is no longer dominant with respect to the natural shear effect. Moreover, the presence of a secondary transversal vortex at the top of the base (centred in F_3) tends to increase the dissymmetry observed without control (Fig. 4) and the position of the attachment point N moves downwards (Fig. 11.a).

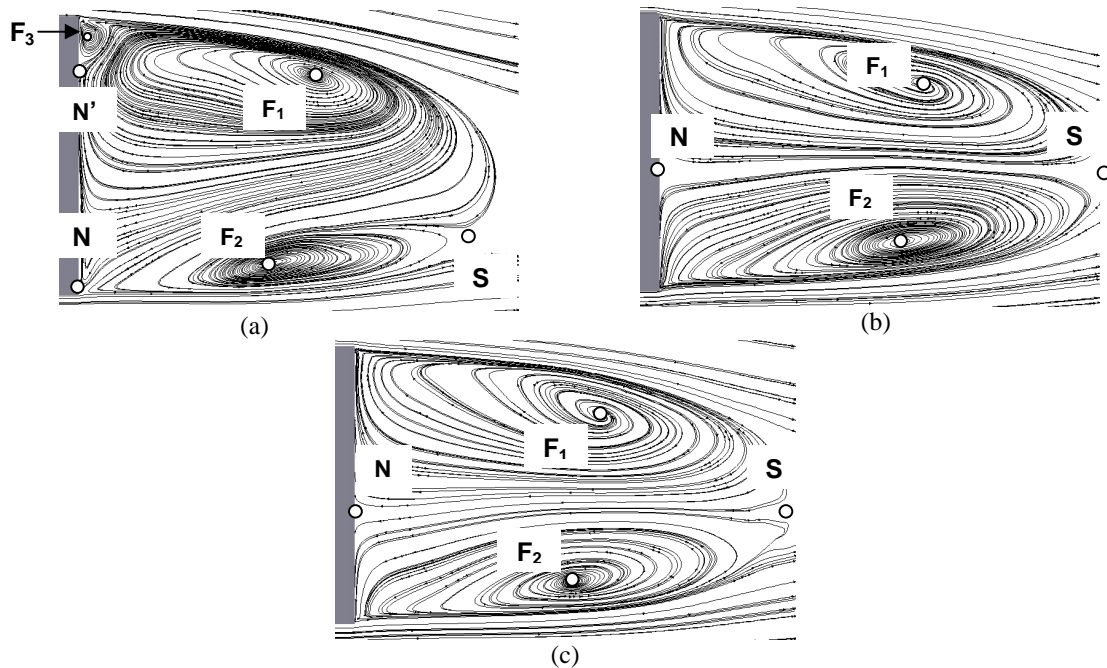


Fig. 11: Time-averaged streamline fields in the wake, on the symmetry plane:(a) $\theta=30^\circ$, (b) $\theta=45^\circ$ and (c) $\theta=60^\circ$

The results presented in Fig. 11 do not however reveal the origin of the drag reductions observed in Fig. 9. The analysis is then conducted according to the expression by Onorato et al. [15] (Eq. (8)). This formula provides an indication of the aerodynamic drag based on values measured in the wake, instead of values measured on the body

surface. By means of momentum applied to the volume described by a current tube enclosing the vehicle surface, it comes:

$$F_x = \int_A (P_{io} - P_i) d\sigma + \frac{1}{2} \rho V_0^2 \left(\int_A \left(\frac{V_y^2}{V_0^2} + \frac{V_z^2}{V_0^2} \right) d\sigma - \int_A \left(1 - \frac{V_x}{V_0} \right)^2 d\sigma \right) \quad (8)$$

Equation (8) associates the drag value with the transversal wake section A (1st, 2nd and 3rd integral), the total pressure losses in the separated structures (1st integral), the rotating kinetic energy in the longitudinal vortices (2nd integral) and the longitudinal velocity deficit in the near-wake flow (3rd integral). Accordingly, the drag reduction requires a reduction in the transversal wake section, a limitation in the longitudinal vortices development and a reduction in the upstream/downstream total pressure losses. Implicitly, the last objective will require an increase of the static pressure distribution locally on the rear part of the body (to limit the pressure drag).

For this purpose, the total pressure loss coefficient profiles are measured in the longitudinal median plane, at $x/H=0.5$ (Fig. 12.a). The mean value of the total pressure loss coefficient along the profile decreases with the control: $C_{pi}=0.934$ without control, $C_{pi}=0.873$ at $\theta=30^\circ$, $C_{pi}=0.823$ at $\theta=45^\circ$ and $C_{pi}=0.847$ at $\theta=60^\circ$. This total pressure loss reduction leads to a decrease of energy loss in the wake, and allows an aerodynamic drag reduction, according to equation (8) (1st integral). The total pressure loss variation in the wake effectively corresponds to the mean drag coefficient variation in Fig. 9.

For each configuration (with or without control), the results reveal two peaks in the total pressure loss coefficient profiles (Fig. 12.a), located at $y/H=0.4$ and $y/H=-0.45$. These maxima correspond to the presence of the shear layer emanating from the base periphery, where the vorticity is high. The transversal wake section is thus characterized by the distance H_d between the 2 extrema (Fig. 12.a). The distances H_d measured without and with control ($\theta=45^\circ$ and $\theta=60^\circ$) are $H_d=0.85H$ and $H_d=0.75H$, respectively, and $H_d=0.8H$ at $\theta=30^\circ$. Actually, the evolution of H_d with θ , confirms the observations indicated in Fig. 9. The transversal wake section reduction seems to be associated with the streamlines deviation near the separation line. According to equation (8), this wake section reduction contributes to the aerodynamic drag reduction observed in Fig. 9.

Moreover, as seen before, the use of blowing devices decreases the averaged total pressure loss coefficient along the profile (Fig. 12.a) and thus reduces the aerodynamics drag. The total pressure losses measured in the recirculation zone are assumed to be mainly due to the presence of a backward flow (see Fig. 5). For this reason, the backward longitudinal velocity evolution with the control is presented in Fig. 12.b (in the longitudinal median plane

at coordinates $x/H=0.5$). The results actually show a reduction in the backward velocity magnitude observed in the recirculation zone center (for $-0.4 < y/H < 0.2$): $V_{x \min} = -0.34V_0$ without control, $V_{x \min} = -0.34V_0$ at $\theta=30^\circ$, $V_{x \min} = -0.23V_0$ at $\theta=45^\circ$ and $V_{x \min} = -0.28V_0$ at $\theta=60^\circ$. The last results give an explanation for the total pressure loss reduction observed in Fig. 12.a.

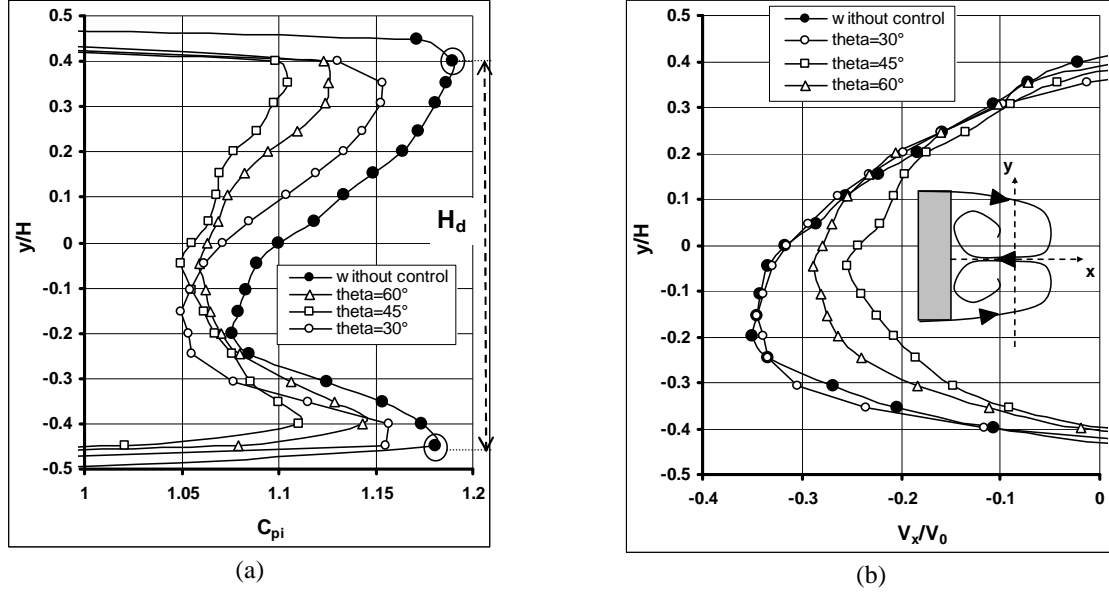


Fig. 12: Vertical profiles measured in the longitudinal median plan at $x/H=0.5$, with and without control: (a) total pressure loss coefficient profile, (b) longitudinal velocity profile.

Further upstream, near the base ($x/H=0.01$), the backward velocity magnitude reduction leads to an increase in the static pressure distribution as shown in Fig. 13 representing the static pressure loss coefficient profile in the longitudinal median plane. Significant static pressure losses appear at coordinates $y/H=-0.5$ and $y/H=0.5$, due to the high velocity near the blowing slots ($V_b=1.5 V_0$). On the contrary, at $-0.45 < y/H < 0.45$, the results show an increase in the static pressure distribution. The time and space averaged static pressure, along the profile, thus tends to increase as the control is applied: $C_p = -0.14$ without control, $C_p = -0.096$ at $\theta=60^\circ$, $C_p = -0.087$ at $\theta=45^\circ$ and $C_p = -0.105$ at $\theta=30^\circ$. Hence, the depression applied via the blowing slots (close to $y/H=0.5$ and $y/H=-0.5$ in Fig. 13) appears to be compensated by the flow recompression at the base center ($-0.45 < y/H < 0.45$ in Fig. 13), and the averaged contribution of the static pressure in the aerodynamic drag decreases. This contribution is implicit in Eq. (8), although it can be expressed through the pressure drag force F_{xp} :

$$F_{xp} = \frac{1}{2} \rho V_0^2 \int_{S_c} C_p \bar{n} \cdot \bar{x} d\sigma \quad (9)$$

Where \bar{n} represents the normal exit line on the geometry.

In conclusion, the drag reductions are mainly due to the wake section reduction, the total pressure loss reduction in the wake, and the static pressure increases on the base. The first point is associated with the streamlines deviation highlighted in Fig. 10. The second and third points are related to the backward velocity magnitude reduction.

The lateral jets contribute at the same way to a drag reduction. Their contribution is however less than of the horizontal jets. If all jets contribute approximately with the same level to a wake surface reduction, the lower horizontal jet has more important effect on the mixing enhancement than the others.

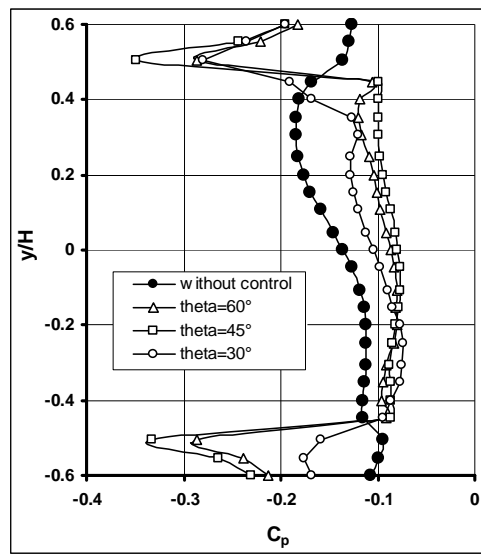


Fig. 13: Static pressure loss coefficient profiles measured in the longitudinal median plane at $x/H=0.01$, with and without control

The control effect can be explained by means of the λ_2 presentation [21]. When the control is applied, the blowing imposes its direction to the shear layer and hence increases the mixing behind the body. Consequently the reattachment length and the wake surface are reduced. In fact, without control the Kelvin Helmholtz vortices move downstream, merge and dissipate. When the control is applied, they move into the recirculation zone and contribute to enhance the mixing. This mechanism leads to a better momentum exchange as can be observed on figure 12.b where the reduction of the negative velocity zone confirms the improvement of the mixing.

When developing active flow control solutions by using an external energy source, it is necessary to ensure that the system runs efficiently, i.e. that the energy used to generate the control is less than the energy saved through aerodynamic drag reduction. Efficiency ζ of the solution is thus evaluated according to equation (10):

$$\begin{cases} \zeta = \frac{P_{ec}}{P_c} \\ P_{ec} = \Delta F_x V_0 \\ P_c = K \frac{\rho V_b^3 S_b}{2} \end{cases} \quad (10)$$

where P_{ec} and P_c represent respectively the energy saved through aerodynamic drag reduction and the energy used to generate the control, K represents a generic total pressure loss [40]. S_b is the blowing surface and ΔF_x is the drag reduction induced by the blowing. The control is considered efficient when the value ζ is equal to or greater than $\zeta_c=1$. Here, the consumed energy is due to the total pressure loss generated through the blowing slot (K_{slot}) and to the losses occurring in the upstream circuit (K_{sys}). Usually during continuous flow through a given orifice, K_{slot} is set to 1.5 to take into account the inlet and outlet effects of the slot (Idel-Cik [41]). Inside the pushing system, the pressure loss K_{sys} is arbitrarily set to 3.5. The total pressure loss coefficient K of the total system is thus equal to 5.

The critical efficiency $\zeta_c=1$ is used to determine a critical coefficient K_c beyond which the control is no longer economically viable.

$$K_c = 2 \frac{\Delta F_x V_0}{\zeta_c \rho V_b^3 S_b} \quad (11)$$

The efficiency coefficient increases when the velocity decreases. For this reason, the jet angle is kept constant and equal to 45° , and lower jet velocities have been tested. Figure (14) presents the drag coefficient as a function of the blowing velocity. The drag reduction increases when the blowing velocity increases. For blowing velocity of $0.5V_0$, the drag reduction is still significant (20%). The efficiency is presented on figure (14). For $V_b/V_0=1.5$ used in this paper the efficiency is equal to 0.4. This curve presents a maximum value of 7 at $V_b/V_0=0.5$, which thus is the best blowing velocity with respect to this criterion. In this case, the saved power compared to the supply power is 7 times higher. The error-bar line segments in Fig.14 are the standard deviation (rms) of the time averaged drag coefficient.

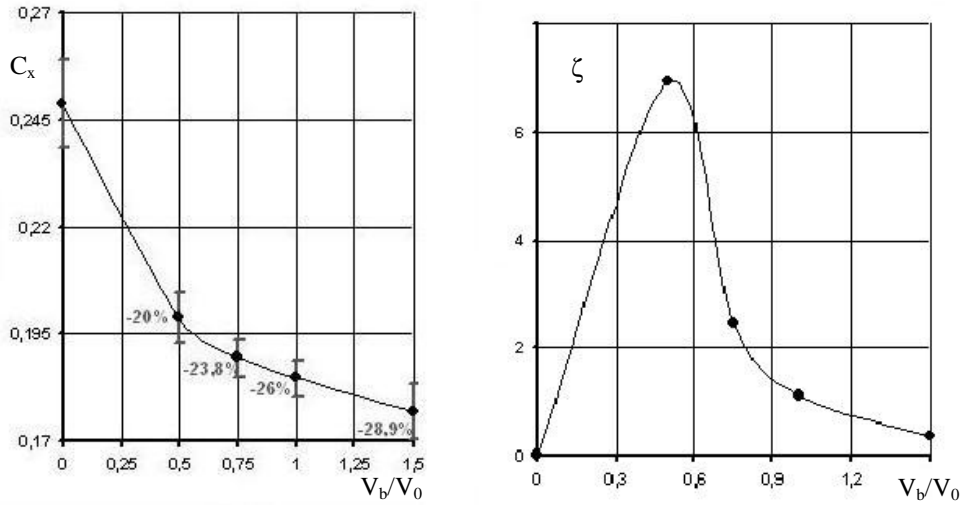


Fig. 14: drag coefficient and control efficiency ζ variations with blowing velocity

IV. Conclusion

An active open-loop flow control using continuous blowing devices has been tested on a simplified square-back geometry, with the goal to reduce the aerodynamic drag. The influence of blowing slots distributed around the base periphery on the near-wake flow topology is analyzed by 3D numerical methods and the obtained aerodynamic drag reductions are discussed.

The near-wake flow topology is first analysed without control. The results are qualitatively in good agreement with previous results and reveal a typical square-back geometry wake. A transversal ring of vortex develops in the near-wake flow, due to the streamline separations around the base periphery, and generates two counter-rotating longitudinal vortices further downstream, due to the interaction with the main flow.

The control is first applied with a blowing velocity of $1.5V_0$. A minimum drag coefficient is obtained for a blowing jet inclination with respect to the vertical plane of $\theta_0=45^\circ$. In this case, 29% of drag reduction is obtained, associated to a significant reduction in the wake section, a total pressure loss reduction in the wake and an increase of the static pressure in the rear part of the geometry.

The efficiency of the control system can be improved by reducing the blowing velocity or by reducing the number, width or lengths of the slots. The first solution is tested at the efficient jet angle $\theta_0=45^\circ$. The cheaper

solution is obtained for the jet velocity of $V_b=0.5V_0$. In this condition, a drag reduction of 20% is obtained with a control energy only seven times smaller than the total energy saved.

Finally, in addition to reduce the wake surface, the oriented blowing jets improve the mixing inside the recirculation zone and hence reduce this same recirculation zone.

Acknowledgements

The authors are thankful to the referees for substantial improvement in the paper due to their careful reviews.

References

- [1] Gad-El-Hak, 1996, Modern developments in flow control, *Applied Mechanics reviews*, **9**, pp. 365-379.
- [2] Gilliéron P., 2002, Contrôle des écoulements appliqués à l'automobile. Etat de l'art, *Mécanique & Industries* 3, pp 515-524.
- [3] Ivanic T. & Gilliéron P., 2004, Reduction of the aerodynamic drag due to cooling system: an analytical and experimental approach, *SAE Paper 2005-01-1017*.
- [4] Tensi J., Boué I. & Paillé F., 1999, Effets comparés sur l'écoulement autour d'un cylindre a faible nombre de Reynolds d'un soufflage pariétal amont et en aval du décollement, *14^{eme} Congrès Français de Mécanique, Toulouse*.
- [5] Hucho W.H., 1998, Aerodynamics of road vehicles- *Ann. Rev. Fluid Mech.* **25**, pp. 485-537
- [6] Castro, I.P. and Robins, A.G., The Flow Around a Surface-Mounted Cube in Uniform and Turbulent Stream, *Journal of Fluid Mechanics*, Feb. 1977, **79**, pp. 307-335.
- [7] Hunt, J.C.R., Abell, C.J., Peterka, J.A, and Woo, H., Kinematical Studies of the Flow Around Free or Surface-Mounted Obstacles: Applying Topology to Flow Visualization, *Journal of Fluid Mechanics*, **86**, July 1978, pp. 179-200.
- [8] Schofield, W.H., and Logan, E., Turbulent Shear Flow over Surface-Mounted Obstacles, *Journal of Fluids Engineering*, **112**, n. 4, 1990, pp. 376-385.
- [9] Larousse, A., Martinuzzi, R., and Tropea, C., Flow Around Surface-Mounted Three Dimensional Obstacles, *9th International Symposium on Turbulent Shear Flow*, Springer-Verlag, 1991, pp.127-139.

- [10] Martinuzzi, R., and Tropea, C., The Flow Around Surface-Mounted Prismatic Obstacles Placed in Fully Developed Channel Flow, *Journal of Fluids Engineering*, **115**, N; 1, 1993, pp. 85-91.
- [11] Hussein, H. and Martinuzzi, R.J., Energy Balance for Turbulent Flow Around Surface Mounted Cube Placed in Channel, *Physics of Fluids*, **8**, 3, 1996, pp. 764-780.
- [12] Kim, T., Lee, B., Lee, D., Hwang, J. and Lee D. H., A Study on Vortex Shedding Around a Bluff Body near The Ground, *SAE Technical Paper Series*, 2003-01-0652.
- [13] Shah, K.B., and Ferziger, J.H., A Fluid Mechanics View of Wind Engineering: Large Eddy Simulation of Flow Past a Cubic Obstacle, *Journal of Wind Engineering and Industrial Aerodynamics*, **67**, April 1997, pp.211-224.
- [14] Krajnovic, S., and Davidson, L., Large Eddy Simulation of the Flow around a Bluff Body, *AIAA Journal*, 40, n. 5, May 2002.
- [15] Onorato M., Costelli A. F. & Garonne A., 1984, Drag measurement through wake analysis, *SAE, SP-569, International Congress and Exposition*, Detroit, MI, february 27 march 2, 1984, pp. 85-93
- [16] McCallen & al, 2000, Aerodynamic drag of heavy vehicles (class 7-8): simulation and benchmarking, *SAE Technical Papers Series* 2000-01-2209
- [17] Bourgois S., Alvi F.S., Tensi J. & Bonnet J.P., 2004, Control of flow separation using microjets, *Proceedings of the First European Forum on Flow Control, Poitiers, 11 au 14 Octobre 2004*.
- [18] Rouméas M., Gilliéron P. & Kourta A., 2008, Separated flows around the rear window of a simplified car geometry, *Journal of Fluid Engineering, Feb 2008 (JFE_06_1229)*.
- [19] Pervaiz M. & Teixeira M., 1999, Two equation turbulence modeling with the lattice-Boltzmann method, proceedings of ASME PVP Division conference, 2nd International Symposium on Computational Technologies for Fluid/Thermal& Chemical systems with industrial applications, Boston.
- [20] Li Y., Shock R., Zhang R. & Chen H., 2004, Numerical study of flow past an impulsively started cylinder by Lattice Boltzmann method, *J. Fluid. Mech.*, 519, pp. 273-300.
- [21] Rouméas, M., 2006, Contribution à l'analyse et au contrôle du sillage épais par aspiration ou soufflage continu., *Thèse de Doctorat, INP Toulouse*.

- [22] Frisch. U, D’Humières U. & Pomeau Y., 1986, Lattice-gas automata for Navier-Stokes equation, *Phys. Rev. Lett*, **56**, pp. 1505-1508.
- [23] Chen S., Chen H. , Martinez D. & Matthaeus W., 1991, Lattice Boltzmann Model for simulation of magnetohydrodynamics, *Phys. Rev. Lett.*, **67**, pp 3776-3779.
- [24] Chen S., Chen H. & Matthaeus W., 1992, Recovery of the Navier-Stokes equations using a lattice-gas Boltzmann method, *Phys. Rev. Ann.*, **45**, R5339-42
- [25] Bhatnagar P.L., Gross E.P. & Krook M., 1954, A model for collision processes in gases. Small amplitude processes in charged and neutral one-component systems. *Phys. Rev.*, **94**(3), pp 511-525.
- [26] Chen H., Teixeira C. & Molvig K., 1997, Digital Physics approach to computational fluid dynamics: some basic theoretical features, *Int. J. Modern Phys. C*, 8(4), pp. 675-684.
- [27] Yakhot V. & Orszag S.A., 1986, Renormalization group analysis of turbulence. Basic theory. *Int J. Sci. Comput*, 1, pp. 1-51
- [28] Pervaiz M. & Teixeira M., 1999, Two equation turbulence modeling with the lattice-Boltzmann method, *proceedings of ASME PVP Division conference, 2nd International Symposium on Computational Technologies for Fluid/Thermal & Chemical systems with industrial applications, Boston.*
- [29] Li Y., Shock R., Zhang R. & Chen H., 2004, Numerical study of flow past an impulsively started cylinder by Lattice Boltzmann method, *J. Fluid Mech.*, **519**, pp273-300.
- [30] Shock R. A., Mallick S., Chen H., Yakhot V. & Zhang R., 2002, Recent results on two dimensional airfoils using lattice Boltzmann-based algorithm, *Journal of Aircraft*, **39** n° 3, May-June 2002
- [31] Chen H., Teixeira C. & Molvig K., 1998, Realization of fluid boundary conditions via discrete Boltzmann dynamics, *International Journal of Modern Physics C*, **9**, No.8, p. 1281
- [32] Yu D., Mai R., & Shyy W., 2002, A multi-block lattice Boltzmann method for viscous fluid flow, *Int. J. Numer. Meth. Fluids*, **39**, pp. 99-120
- [33] Ahmed S. R., Ramm R. & Falting G., 1984, Some salient features of the time averaged ground vehicle wake, *SAE technical paper series 840300*, Detroit 1984
- [34] Duell E.G. & George A.R., Experimental study of a ground vehicle body unsteady near wake, SAE Paper 1999-01-0812, Detroit, USA, 1999

- [35] Krajnovic S. & Davidson L., 2003, Numerical study of the flow around the bus-shaped body, *ASME Journal of Fluid Engineering*, **125**, pp. 500-509.
- [36] Huchot, W.-H., 1998, Aerodynamics of Road Vehicles (4th ed.), *Society of Automotive Engineers, Inc.* ISBN 0-7680-0029-7.
- [37] Chometon L. & Gilliéron P., 1996, Modélisation des écoulements tridimensionnels décollés autour des véhicules automobiles à l'aide d'un modèle à zéro-dimension, *Journée d'étude SIA « Aérodynamique – Aéroacoustique - Aérothermique automobile et ferroviaire »*, Courbevoie-Paris 5 et 6 novembre 1996, n° 96-09-11.
- [38] Kourta A. Boisson H.C., Chassaing P., HaMinh H., 1987, Non-linear interaction and the transition to turbulence in the wake of a circular cylinder, *Journal of Fluid Mechanics*, **181**, pp. 141-161.
- [39] Kourta A., 2004, Instability of channel flow with fluid injection and parietal vortex shedding, *Computers and Fluids*, **33**, 2, pp 155-178.
- [40] Lehugeur B., Gilliéron P. & Ivanic T., 2006, Contribution de l'éclatement tourbillonnaire à la réduction de la traînée des véhicules automobiles: approche numérique, *C.R. Mécanique* **334** pp. 368-372.
- [41] Idel-Cik I. E., 1986, Memento des pertes de charges, Ed. Eyrolles, Paris, 1986.